

Ab initio calculation of the OH (X^2_{Π} , $A^2_{\Sigma^+}$)+Ar potential energy surfaces and quantum scattering studies of rotational energy transfer in the OH ($A^2_{\Sigma^+}$) state

Alessandra Degli Esposti and Hans-Joachim Werner

Citation: *The Journal of Chemical Physics* **93**, 3351 (1990); doi: 10.1063/1.458816

View online: <http://dx.doi.org/10.1063/1.458816>

View Table of Contents: <http://aip.scitation.org/toc/jcp/93/5>

Published by the *American Institute of Physics*



**COMPLETELY
REDESIGNED!**

**PHYSICS
TODAY**

Physics Today Buyer's Guide
Search with a purpose.

Ab initio calculation of the OH ($X^2\Pi$, $A^2\Sigma^+$) + Ar potential energy surfaces and quantum scattering studies of rotational energy transfer in the OH ($A^2\Sigma^+$) state

Alessandra Degli Esposti^{a)} and Hans-Joachim Werner

Fakultät für Chemie, Universität Bielefeld, 4800 Bielefeld, Federal Republic of Germany

(Received 6 February 1990; accepted 5 April 1990)

The potential energy surfaces of OH + Ar, which correlate asymptotically with OH($X^2\Pi$) + Ar(1S) and OH($A^2\Sigma^+$) + Ar(1S), have been calculated using the coupled electron pair approximation (CEPA) and a very large basis set. The OH–Ar van der Waals complex is found to be bound by about 100 cm^{-1} in the electronic ground state. In agreement with several recent experimental studies **the first excited state is found to be much more stable.** **The A state potential energy surface has two minima at collinear geometries** which correspond to isomeric OH–Ar and Ar–OH structures. The dissociation energies D_e are calculated to be 1100 and 1000 cm^{-1} , respectively; both forms are separated by a barrier of about 1000 cm^{-1} . The equilibrium distances for OH–Ar and Ar–OH are calculated to be 2.9 and 2.2 Å , respectively, relative to the center of mass of OH. In order to investigate the nature of the strong binding in the A state, we have calculated accurate dipole and quadrupole moments as well as dipole and quadrupole polarizabilities for the X and A states of the OH radical and for the Ar atom. These data are used to estimate the contributions of induction and dispersion forces to the long-range OH–Ar potential. The calculated potential energy surfaces have been fitted to an analytical function and used in quantum scattering calculations for collision induced rotational energy transfer in the A state of OH. From the integral cross sections rate constants have been evaluated as a function of the temperature. The theoretical rate constants are considerably larger than the corresponding experimental values of Lengel and Crosley [J. Chem. Phys. **67**, 2085 (1977)], but in good agreement with recent measurements of Jörg, Meier, and Kohse-Höinghaus [J. Chem. Phys. (submitted)]. Our potential energy surface has also been used to calculate the bound rovibrational levels of the OH–Ar complex.

I. INTRODUCTION

Recently, several groups have observed and spectroscopically characterized a surprisingly stable OH($A^2\Sigma^+$) + Ar(1S) van der Waals complex in the gas phase.^{1–3} **This complex was so far known only in an Ar matrix.**⁴ Using laser induced fluorescence (LIF) Berry, Brustein, Adamo, and Lester¹ monitored excitation spectra in the region of the OH($A^2\Sigma^+$, $v' = 0 \leftarrow X^2\Pi_{3/2}$, $v'' = 0$) transition. In a supersonic expansion and in the presence of Ar they observed ten new features, seven of which were assigned to a vibrational progression of the OH–Ar stretching mode in the excited state. A similar experiment was carried out by Fawzy and Heaven,³ who observed six of the bands. Berry, Brustein, and Lester² analyzed the rotational structure of the fluorescence excitation spectrum assuming a collinear structure of the van der Waals complex. For the A state they derived an OH–Ar distance of 2.9 Å (relative to the center of mass of OH), a vibrational constant $\omega_e = 170\text{ cm}^{-1}$, and an anharmonicity constant $\omega_e x_e = 9.0\text{ cm}^{-1}$. The dissociation energy D_0 was determined to be 718 cm^{-1} . The latter value depends on the assignment of the bands and a linear Birge–Sponer extrapolation, which is somewhat uncertain.

A different kind of experiment was reported by Le-maire, Tchang-Brillet, Shafizadeh, Rostas, and Rostas.⁵ These authors observed an excimer fluorescence spectrum of OD–Ar, which was produced by two-photon photodissociation of D_2O in the presence of argon. The spectrum was analyzed by assuming a simple collinear Franck–Condon model. However, this model could not satisfactorily explain the observed intensity profile. **This indicates that nonlinear structures and two-dimensional rovibrational wave functions must be considered in order to obtain realistic Franck–Condon factors and intensity profiles.**

These new experiments provide for the first time direct experimental information about the OH–Ar (X,A) potential energy surfaces. Most interestingly, the van der Waals complex in the excited state is about 10 times more strongly bound than in the ground state, and the equilibrium distance of the A state complex reported by Berry *et al.*² ($r_e = 2.9\text{ Å}$) is considerably shorter than that of the ground state ($r_e = 3.6\text{ Å}$). These potentials are relevant for the dynamics of collision induced rotational energy transfer, as studied experimentally by Lengel and Crosley⁶ and Jörg, Meier, and Kohse-Höinghaus⁷ for the $A^2\Sigma^+$ electronic state of OH.

The purpose of the present paper is to calculate as accurately as possible the potential energy surfaces of the OH($A^2\Sigma^+$, $X^2\Pi$) + Ar system using highly correlated *ab initio* wave functions. These calculations will give, for the first time, information about the global form of the interac-

^{a)} Permanent address: Istituto di Spettroscopia Molecolare—C.N.R., Via de' Castagnoli, 1, 40126 Bologna (Italy).

tion potential and will provide insight in the origin of the strong binding in the A state. Our potential energy surfaces have been employed in quantum scattering calculations describing collision induced rotation energy transfer (RET) in the A state. A similar study of RET in the $X^2\Pi$ state will be represented in a future publication. Two-dimensional calculations of the bound rovibrational states of the van der Waals complex and simulations of the observed fluorescence excitation spectra and of the excimer fluorescence spectra have also been performed and will be presented in a separate paper.⁸

II. AB INITIO CALCULATIONS

The potential energy surface of the OH–Ar complex is a function of the bond distance r of the OH molecule, the distance R of the argon atom from the center of mass of the OH molecule, and the angle θ between the molecular axis and the center of mass–Ar axis. $\theta = 0$ corresponds to the linear OH–Ar structure. In our calculations we have assumed a fixed OH distance of $r = 1.95$ bohr, which corresponds to the average distance r_0 of the ($A^2\Sigma^+$, $v' = 0$) state.

The long range part of the interaction potential can be represented by a multipole expansion

$$V(R, \theta) = \sum_n c_n(\theta) R^{-n}, \quad (1)$$

where the c_6 , c_7 , and c_8 constants can be approximated in terms of the dipole moment μ , the quadrupole moment Θ , the dipole and quadrupole polarizability tensors α , \mathbf{A} , and \mathbf{C} of the OH radical, as well as the dipole and quadrupole polarizabilities α and C , respectively, of the Ar atom.⁹ It is therefore essential that the electronic wave functions employed reproduce these quantities as accurately as possible. In order to calculate reliable polarizabilities, it is generally important to use a flexible s, p basis set.¹⁰ The dipole polarizability requires additional d polarization functions, and the quadrupole polarizability requires f functions. For the calculation of the OH–Ar surface it was necessary to make a compromise between basis set size and accuracy. The d and f functions used in the final calculations were therefore carefully optimized to reproduce as accurately as possible the dipole and quadrupole polarizabilities of the fragments as obtained with considerably larger basis sets.

In addition to the diffuse f functions needed to obtain accurate quadrupole polarizabilities, tighter f functions, which were roughly energy optimized, were included in the basis sets for O and Ar. These functions considerably improve the calculated ionization energy of Ar and the electron affinity of OH. They also somewhat reduce the polarizabilities since their effect on the electron correlation leads to a slight contraction of the electron distribution.

The oxygen s, p GTO basis set was derived from the energy optimized 13s, 8p set of van Duijneveldt;¹¹ the most diffuse s function of this basis was replaced by two s functions with exponents 0.208 and 0.087 (all exponents given in bohr⁻²), and the most diffuse p function was replaced by

two functions with exponents 0.135 and 0.054. The innermost eight s and four p functions were contracted. For hydrogen, we used the van Duijneveldt 8s basis, which was augmented by a further s function with exponent 0.03. The innermost 5 s functions were contracted. The argon basis was derived from the 16s, 12p basis of Partridge;¹² a further s function with exponent 0.07 was added, and the last two p functions were replaced by three functions with exponents 0.284, 0.123, and 0.053. The first 12 s functions were generally contracted to two functions, using the coefficients of the 1s and 2s orbitals of an uncontracted SCF calculation. The addition of further s or p functions to this basis set or a change of the contraction scheme had virtually no effect on the calculated dipole and quadrupole moments, polarizabilities, and OH–Ar interaction energies.

The final basis set for oxygen contained four d functions with exponents 3.6, 1.2, 0.3, and 0.1, and two f functions with exponents 1.4 and 0.14; the first two d functions were contracted with coefficients (0.125 939 and 0.642 522). These coefficients were taken from the first δ natural orbital of a CEPA calculation for OH. On the hydrogen atom we added a d function with exponent 0.5. The final basis for Ar contained four d functions with exponents 2.52, 0.84, 0.28, and 0.093; the first two of these were contracted with coefficients (0.137 646 and 0.630 10). Two f functions with exponents 0.9 and 0.14 were added. In total this basis set consisted of 130 contracted GTOs.

In Table I we present a comparison of the calculated multipole moments and polarizabilities for the $A^2\Sigma^+$ state of OH for the final basis set described above (basis A) and a considerably larger basis set (B) with 4d, 4f on oxygen and 4p, 3d on hydrogen (exponents see below Table I) with previous calculations¹³ and experimental data.^{14,15} The definition of all quantities can be found in Ref. 9. All values were obtained as first or second derivatives of the energy with respect to finite electric fields F_α or field gradients $F_{\alpha\beta}$. The energies were calculated within the coupled electron pair approximation^{16,17} (CEPA). It is known that this approximation, which includes all single and double excitations out of the Hartree–Fock wave function and accounts for higher order excitations approximately, yields very accurate potential energy functions and molecular properties for the first row hydrides.^{17–20} It is found that the dipole and quadrupole moments, as well as the dipole polarizabilities differ by less than 0.5% for both basis sets. The \mathbf{A} and \mathbf{C} tensors differ by up to about 5%. For comparison, some results of previous calculations are also shown in Table I. It is noted that all values given are evaluated for an OH bond distance of 1.95 bohr, which is the average distance r_0 for the A state. The values for this state should therefore be good approximations to the vibrationally averaged quantities for $v = 0$. The r_0 value for the ground state of OH is considerably shorter. Therefore, the values given in Table I are not compared to the experimental values for the ground state, but such a comparison for calculations of comparable quality can be found in our previous papers.^{20,21} A similar comparison is made in Table II for the polarizabilities of Ar. Again basis A is the one used in our final calculations, while basis B is much bigger and included 5d, 5f, and 2g functions. It is found that

TABLE I. Calculated multipole moments and polarizabilities^a for the OH $X(^2\Pi)$ and $A(^2\Sigma^+)$ states at a bond distance of 1.95 bohr (all values in a.u.).

State	Basis ^b	μ	Q_{zz}	α_{zz}	α_{yy}	$A_{z,zz}$	$A_{x,xz}$	$C_{zz,zz}$	$C_{yy,yy}$	$C_{yz,yz}$
$X(^2\Pi)$	<i>A</i>	0.654	1.391	9.42	7.02	8.29	1.48	15.46	10.96	9.84
	Previous calc. ^c									
	Ref. 13	0.650	1.49							
	Ref. 20	0.655								
$A(^2\Sigma^+)$	<i>A</i>	0.735	3.184	8.70	8.31	6.14	3.07	13.96	13.91	6.82
	<i>B</i>	0.738	3.184	8.71	8.31	6.17	3.23	14.22	14.56	7.31
	Experimental ^d									
	Ref. 14	0.676 ± 0.04								
	Ref. 15	0.849 ± 0.03								
	Previous calc. ^c									
	Ref. 13	0.745	3.265							

^a μ is the dipole moment, Q the quadrupole moment, and α , A , and C are the dipole, dipole-quadrupole, and quadrupole polarizabilities, respectively. For definitions see Ref. 9. The OH bond lies along the z axis. All quantities have been calculated as energy derivatives using finite fields of ± 0.005 a.u. and CEPA (1) wave functions.

^b Basis *A*: final basis set (see the text); Basis *B*: same s , p basis as in *A*, but larger set of polarization functions: d_O (2.2,0.73,0.24,0.08), f_O (1.2,0.427,0.107,0.035), p_H (1.2,0.35,0.12,0.04), and d_H (0.60,0.2,0.07).

^c Calculated at $r = 1.95$ bohr.

^d Experimental values for $v = 0$.

the calculated dipole polarizabilities differ by less than 1% and are in very close agreement with the experimental values^{22–24} and previous calculations.^{25,26} As for OH, the quadrupole polarizabilities obtained with both basis sets differ by about 5%. Our calculated C values are in good agreement with a previous calculation of Cernusak *et al.*²⁵

If the two sets of constants in Tables I and II are used to calculate the induction plus approximate dispersion energy of OH–Ar (cf. Sec. IV), the difference in the interaction energy at a distance of 4 Å is about 2%, irrespective of the angle θ . This error increases with decreasing OH–Ar distance, but we feel that it is small as compared to other uncertainties in our calculation of the OH–Ar surface.

Since long-range dispersion forces between atoms and molecules are due purely to electron correlation effects, it is necessary to use highly correlated electronic wave functions in order to obtain reliable potential energy surfaces of van der Waals complexes. It is advantageous to use a size-consistent method, since then the calculated difference between the complex energy and the fragment energies vanishes at

large atom–molecule distances. It is also important to correct for basis superposition errors (BSSE), which are due to the fact that the basis sets of the fragments are not complete. The BSSE can be reduced by applying the counterpoise correction (CPC), as originally suggested by Boys and Bernardi.²⁷ The counterpoise correction for our OH–Ar system is defined as

$$\Delta E_{cp}(R, \theta, r) = E_{OH}(\infty, r) - E_{OH}(R, \theta, r) + E_{Ar}(\infty) - E_{Ar}(R, \theta, r), \quad (2)$$

where $E_{OH}(\infty, r)$ and $E_{Ar}(\infty)$ are the separately calculated fragment energies. $E_{OH}(R, \theta, r)$ is the OH energy obtained with the additional Ar basis functions positioned at R, θ , and $E_{Ar}(R, \theta, r)$ is the Ar energy calculated with the additional OH basis functions at the geometry defined by R, θ , and r . The total interaction energy is defined as

$$V(R, \theta, r) = E_{OH-Ar}(R, \theta, r) - E_{OH}(\infty, r) - E_{Ar}(\infty) + \Delta E_{cp}(R, \theta, r) - \Delta E_{sc}(r), \quad (3)$$

where $\Delta E_{sc}(r)$ is a size consistency correction, which is assumed to be independent of R and θ , and given by

$$\Delta E_{sc}(r) = E_{OH-Ar}(\infty, r) - E_{OH}(\infty, r) - E_{Ar}(\infty). \quad (4)$$

For size consistent wave functions $\Delta E_{sc} = 0$, but for most types of variational configuration interaction wave functions $\Delta E_{sc} > 0$.

In order to study the basis set dependence of ΔE_{cp} and $V(R, \theta, r)$ we have performed a number of test calculations at collinear OH–Ar geometry with $R = 2.9$ Å and $r = 1.95$ Å, i.e., near the equilibrium geometry of the *A* state complex. Table III shows a comparison of interactions energies and counterpoise corrections obtained with different basis sets and CEPA wave functions. The interaction energy calculated without f functions is smaller by about 15% than the value obtained with the largest basis. Addition of both the diffuse and the energy optimized f functions increases the interaction energy by about 3%. Also the addition of d func-

TABLE II. Dipole (α) and quadrupole (C) polarizabilities of argon (in a.u.).

Method	Basis ^a	α	C
CEPA(1)	<i>A</i>	11.06	24.86
CEPA(1)	<i>B</i>	11.15	26.10
<i>Experimental</i>			
Ref. 22		11.074	
Ref. 23		11.080	
<i>Previous calc.</i>			
Ref. 25 ^b		11.23	26.79
Ref. 26 ^c		11.10	

^a Basis *A*: final basis set, see the text; Basis *B*: same s , p basis as in *A* but larger set of polarization functions: d (2.52,0.84,0.28,0.11,0.045), f (2.52,0.84,0.28,0.11,0.045), g (0.3,0.1).

^b Finite-field MBPT(4) calculation.

^c Finite-field CEPA calculation.

TABLE III. Comparison of interaction energies V , counterpoise corrections (ΔE_{cp}), and size consistency corrections (ΔE_{sc}) for the linear^a OH-Ar $A^2\Sigma^+$ complex (all values in cm^{-1}).

Method	Basis ^b	V	ΔE_{cp}	ΔE_{sc}
CEPA(1)	C	-954.7	410.4	0
CEPA(1)	D	-980.7	402.5	0
CEPA(1)	E	-1012.6	200.7	0
CEPA(1)	A	-1090.1	243.2	0
CI(SD)	A	-771.8	226.1	4963
MR(CI) ^c	A	-769.9	227.5	3322

^a $r = 1.95$ bohr, $R = 5.48$ bohr.

^b Basis C : final s, p, d basis set, see the text; Basis D : as C plus $1f_O$ (0.14) and $1f_{Ar}$ (0.14); Basis E : as C plus $2f_O$ (0.14, 1.4) and $2f_{Ar}$ (0.14, 0.9); Basis A : as E plus $1d_H$ (0.5) (final basis set).

^c Internally contracted MRCI with 208 reference configurations, see the text. The orbitals are optimized for the $A^2\Sigma^+$ state.

tion on the hydrogen has a significant effect on the interaction energy. It is found that the diffuse f functions have hardly any effect on the CPC, while the inclusion of the tighter second set of f functions reduces the CPC by about a factor of 2. It is satisfying to see that the calculated counterpoise corrected interaction energy changes by only about 30 cm^{-1} , while the CPC changes by 200 cm^{-1} . This indicates that the counterpoise method does not greatly overestimate the BSSE.

Table III also shows a comparison of the CEPA interaction energies with the corresponding variational CI(SD) values. Since the latter method is not size consistent, ΔE_{sc} is also given. The CI(SD) interaction energy is about 30% smaller than the CEPA interaction energy, indicating that higher order excitations are important to describe the binding of the complex. In order to investigate the effect of higher order excitations in more detail, we have performed a number of multireference CI calculations, in which the reference was a complete active space SCF (CASSCF) wave function, with the Ar orbitals and the OH 1σ orbitals inactive (doubly occupied), and the OH orbitals $2\sigma-4\sigma$, 1π , 2π active (198 CSFs at collinear geometry, calculated in C_{2v} symmetry). The corresponding internally contracted²⁸ MRCI wave functions included all single and double excitations out of the 11 valence orbitals of this MCSCF reference wave function. Since the MCSCF function contains the most important singly and doubly excited configurations relative to the Hartree-Fock (RHF) wave function of OH, the MRCI also accounts for the most important triple and quadrupole excitations out of the OH orbitals. This leads to a reduction of the size consistency error by about 25% as compared to the simple CI(SD) wave functions. However, as seen in Table III, the calculated interaction energy is very similar to the one obtained with the CI(SD) wave function. The large difference between the CI and the CEPA results is therefore probably due to the effect of higher order excitations involving Ar orbitals. Unfortunately, it was not possible to include excitations into virtual Ar orbitals in the reference wave function. For Ar the excitations into the $3d$ orbitals are energetically most important, while excitations into the $4s$ and $4p$ account for relaxation and polarization effects. Thus, in a

good MRCI calculation one would have to include nine more orbitals into the active orbital set. Such calculations would be prohibitively expensive.

The importance of higher order excitations in the CI wave function and the accuracy of the CEPA approximation can be tested more accurately for the smaller OH-He system. Table IV shows a comparison of the interaction energies obtained with CI(SD), CEPA, and various kinds of MRCI wave functions. The reference wave function of the first MRCI calculation included all single and double excitations out of the valence orbitals of the OH-He Hartree-Fock wave function into the OH orbitals 4σ and 2π . This calculation is similar to the MRCI for OH-Ar mentioned above, except that a CASSCF reference function was used in the latter case. As for OH-Ar, this MRCI yields almost the same interaction energies as the simple CI(SD) calculation. In the second MRCI calculation also single and double excitations into the He $2s$ orbitals were included (229 reference CSFs in C_{2v} symmetry). Finally, in the third MRCI calculation all single and double excitations into the He $2p$ orbitals (639 reference CSFs in C_{2v} symmetry) were added to the reference function. In all cases the orbitals were optimized in MCSCF calculations in which the configuration space was a direct product of the CASSCF wave functions for OH with the orbitals $2\sigma-4\sigma$, 1π , and 2π active and for He with the orbitals ($1s$), ($1s, 2s$), or ($1s, 2s, 2p$) active. The optimization for CASSCF reference functions was not possible, since then an OH 5σ orbital was obtained instead of the He $2s$ orbital. The two large MRCI calculations yield potentials which are considerably more attractive than the CI(SD) potential. The contribution of excitations into the He $2p$ orbitals in the reference function is quite small, even though the size consistency correction is much reduced in the calculations with the He $2p$ orbitals active. It is found that the

TABLE IV. Comparison of interaction energies (in cm^{-1}) for OH + He ($\theta = 0^\circ$, $r_{OH} = 1.95$ bohr).

$R(\text{a.u.})$	CI(SD)	MRCI ^a	MRCI ^b	MRCI ^c	CEPA
30 ^d	755.0	508.9	291.6	60.8	0.0
7.0	-32.0	-32.8	-34.2	-38.4	-35.2
6.0	-73.0	-74.8	-82.6	-84.6	-81.2
5.5	-91.6	-93.9	-111.7	-114.7	-105.1
5.0	-57.5	-60.0	-80.5	-93.7	-80.7
4.5	199.1	196.5	168.4	146.1	157.4

^a Reference function includes all singles and doubles into OH($4\sigma, 2\pi$) orbitals. Orbitals from an MCSCF in which the configuration space was a direct product of a CASSCF for OH with $2\sigma-4\sigma$, 1π , 2π active, and the SCF wave function for He. The 1σ orbital is doubly occupied in all configurations.

^b Reference function includes all singles and doubles into OH($4\sigma, 2\pi$) and He ($2s$) orbitals. Orbitals from an MCSCF in which the configuration space was a direct product of a CASSCF for OH with $2\sigma-4\sigma$, 1π , 2π active, and a CASSCF for He with $1s$ and $2s$ active.

^c Reference function includes all singles and doubles into OH($4\sigma, 2\pi$) and He ($2s, 2p$) orbitals. Orbitals from an MCSCF in which the configuration space was a direct product of a CASSCF for OH with $2\sigma-4\sigma$, 1π , 2π active, and a CASSCF for He with $1s, 2s, 2p$ active.

^d The interaction energy at 30 bohr is the size consistency correction which is subtracted from the calculated interaction energies at shorter distances.

largest MRCI calculation yields a well depth which is about 5% deeper than the CEPA value. This could be due to effects of triple excitations which are not accurately accounted for in the CEPA calculation. In view of the results obtained for OH–He we believe that the CEPA interaction potentials calculated for OH–Ar are more reliable than the CI(SD) potentials.

As will be shown later, the binding in the A state is partly due to charge transfer from Ar to OH. In order to describe this effect reliably, it is necessary to obtain the OH electron affinity and the Ar ionization potential as accurately as possible. Both quantities are strongly influenced by electron correlation effects, and it is therefore difficult to calculate them with an accuracy better than about 0.2 eV. However, as seen from the results in Table V, the difference of the ionization potential of Ar and the electron affinity of the OH A state is obtained with high accuracy, due to almost equal errors in both quantities. Since it is expected that the importance of charge transfer depends mainly on this difference, it is hoped that the effect is well described in our calculations.

III. ANALYTICAL REPRESENTATION OF THE OH–Ar POTENTIALS

The OH–Ar A state is represented by a single interaction potential energy surface which we denote as $V_\Sigma(R, \theta, r)$. However, two surfaces are needed to characterize the states which correlate with the OH ($X^2\Pi$) state. **This is due to the fact that the asymptotically degenerate $|^2\Pi_x\rangle$ and $|^2\Pi_y\rangle$ states split into two states of A' and A'' symmetry, respectively, if the $C_{\infty v}$ symmetry is lifted by the approach of the Ar atom** (here we neglect the spin–orbit splitting, which is assumed to be geometry independent). These two surfaces will be denoted $V_{\Pi_x}(R, \theta, r)$ (A') and $V_{\Pi_y}(R, \theta, r)$ (A''). The dependence on the angle θ of these three potentials can be expanded as^{31,32}

$$V_\Sigma(R, \theta, r) = \sum_{l=0}^{\infty} V_\Sigma^l(R, r) d_{00}^l(\theta) \quad (5)$$

and

$$\begin{aligned} V_{\Pi_{x,y}}(R, \theta, r) &= V_{\Pi}(R, \theta, r) \mp V_2(R, \theta, r) \\ &= \sum_{l=0}^{\infty} V_{\Pi}^l(R, r) d_{00}^l(\theta) \\ &\quad \mp \sum_{l=2}^{\infty} V_2^l(R, r) d_{20}^l(\theta). \end{aligned} \quad (6)$$

Here d_{mn}^l is a reduced rotation matrix element,³¹ and in Eq. (6) the minus sign is associated with the V_{Π_x} potential. We

TABLE V. Calculated and experimental electron affinities (E.A.) of OH ($A^2\Sigma^+$) and ionization potentials (I.P.) of Ar ($1S_0$) (in eV).

	E.A.	I.P.	I.P. – E.A.
CEPA(1)	5.652	15.530	9.978
Exp.	5.877 ^a	15.759 ^b	9.971

^a Reference 29.

^b Relative to the Ar⁺ ($^2P_{3/2}$) state, Ref. 30.

neglect any collision-induced, nonadiabatic mixing of the A' components of the $^2\Sigma^+$ and $^2\Pi_x$ states, which would be responsible for electronic quenching of the $A^2\Sigma^+$ state.^{31–33} Note that V_2 , as defined in Eq. (6), is equal to one-half the splitting between the A'' (Π_y) and A' (Π_x) potential energy surfaces. As discussed by Dagdigian *et al.*,³⁴ for collisions of $^2\Pi$ molecules with π^3 electron occupancy as here for OH ($X^2\Pi$), at nonlinear geometries the A'' potential will be more repulsive than the A' potential, so that we anticipate V_2 to be positive.

The significance of the V_{Π} and V_2 potentials becomes clearer if the complex angular momentum eigenfunctions

$$|\Pi_+\rangle = -2^{-1/2}(|\Pi_x\rangle + i|\Pi_y\rangle), \quad (7)$$

$$|\Pi_-\rangle = 2^{-1/2}(|\Pi_x\rangle - i|\Pi_y\rangle) \quad (8)$$

are considered. Then we get

$$\begin{aligned} V_{\Pi}(R, \theta, r) + T_{\Pi}(r) &= \langle \Pi_+ | H_{el} | \Pi_+ \rangle \\ &= \langle \Pi_- | H_{el} | \Pi_- \rangle, \end{aligned} \quad (9)$$

$$V_2(R, \theta, r) = \langle \Pi_+ | H_{el} | \Pi_- \rangle = \langle \Pi_- | H_{el} | \Pi_+ \rangle, \quad (10)$$

where H_{el} is the spin-free electronic Hamiltonian and $T_{\Pi}(r)$ is the potential energy function of the isolated OH radical. Hence, V_{Π} describes the change of the two degenerate diagonal matrix elements of the electronic Hamiltonian as a function of the complex geometry relative to the asymptotic ($R \rightarrow \infty$) energy, while V_2 describes the coupling of the two states in this diabatic representation. The theory for collision induced transitions in $^2\Pi$ states has been worked out in detail by Alexander and co-workers.^{35–37} This theory shows that, in Hund's case (*a*), V_2 induces transitions between the rotational manifolds of the $^2\Pi_{1/2}$ and $^2\Pi_{3/2}$ states, while the anisotropy of the V_{Π} potential induces rotational transitions within each spin–orbit manifold.

As noted in Sec. II, the OH–Ar potential has only been calculated for a single OH bond distance $r_0 = 1.95$ bohr. In the following we therefore omit the r dependence of the interaction potentials. The potentials $V_\Sigma(R, \theta)$, $V_{\Pi}(R, \theta)$, and $V_2(R, \theta)$ were fitted to the functional form

$$\begin{aligned} V(R, \theta) &= \sum_{l=1}^L d_{m0}^{l+m-1}(\cos \theta) a_l(R) \\ &= \mathbf{p}^T \cdot \mathbf{a}(R), \end{aligned} \quad (11)$$

where the expansion coefficients $a_l(R)$ correspond to the coefficients $V_\Sigma^l(R)$, $V_{\Pi}^l(R)$, and $V_2^l(R)$ in Eqs. (5) and (6), and L equals the number of angles θ for which the potential has been calculated. As in Eqs. (5) and (6) we have $m = 0$ for the V_Σ and V_{Π} potentials, and $m = 2$ for the V_2 potential. The vector \mathbf{p} has the elements

$$p_l = d_{m0}^{l+m-1}(\cos \theta). \quad (12)$$

The vector \mathbf{a} can be expressed as

$$\mathbf{a}(R) = \mathbf{P}^{-1} \cdot \mathbf{b}(R), \quad (13)$$

where

$$P_{lk} = d_{m0}^{l+m-1}(\cos \theta_k). \quad (14)$$

θ_k are the angles for which the potential has been calculated.

TABLE VI. CEPA(1) interaction potential V_Σ (in cm^{-1}) of OH + Ar as function of R (in Å) and θ (in degrees).^a

R	θ				
	0	45	90	135	180
1.7					10 868.62
1.8					5193.41
1.9					1863.30
2.0		16 777.59	19 431.32	10 725.67	67.79
2.1	19 757.64				- 749.53
2.2					- 983.45
2.3	5274.98				- 930.55
2.5	387.26	1929.38	3417.65	1378.80	- 630.95
2.6	- 534.08				
2.7	- 960.10	669.10	1575.22	564.91	
2.8	- 1101.91				- 353.87
2.9	- 1090.09	133.34	667.47	176.73	- 302.90
3.0	- 1003.32				- 261.68
3.2	- 765.47	- 119.46	117.78	- 37.52	- 196.62
3.3	- 650.97				
3.4					- 146.85
3.5	- 459.72	- 143.92	- 42.13	- 78.15	- 126.56
3.6	- 384.03	- 136.03	- 60.15	- 77.60	- 108.94
3.7	- 320.34	- 125.39	- 66.63	- 74.09	- 93.73
3.8	- 267.17	- 113.61	- 64.37	- 68.95	- 80.65
3.9	- 223.02				
4.0	- 186.48	- 90.27	- 54.62	- 56.97	- 59.86
4.5	- 79.54	- 46.92	- 33.01	- 31.46	- 29.30
5.0	- 37.01	- 24.16	- 18.12	- 17.18	- 15.27
5.5		- 12.94	- 9.99	- 9.29	
6.0	- 10.23	- 7.30	- 5.73	- 5.39	- 4.95
7.0	- 3.60	- 2.69	- 2.14	- 2.07	- 1.96

^a The OH bond distance is fixed at $r = 1.95$ bohr. R is the distance from the Ar atom to the center of mass of OH. θ is the angle between the r and R vectors. $\theta = 0^\circ$ and $\theta = 180^\circ$ correspond to the linear OH-Ar and Ar-OH structures, respectively.

At each angle θ_k the R -dependent potentials are fitted independently to functions of the form

$$b_l(R) = \exp[-a_l(R - R_l)] \cdot \left[\sum_{i=0}^3 b_l^{(i)} R^i \right] - \frac{1}{2} \{1 + \tanh[(R - S_l)/T_l]\} \times \left[\sum_{i=3}^4 c_l^{(2i)} R^{-2i} \right]. \quad (15)$$

The parameters a_l and R_l were determined for each angle from the energies at the two shortest OH-Ar distances R , assuming an exponential R dependence at short range. The parameters S_l and T_l control the switching function which damps the long range part at small R and have been roughly optimized for each angle θ_k . The parameters b_l and c_l are obtained for fixed R_l , S_l , and T_l by a least square fitting procedure.

In the above fitting procedure, the number of terms in the angular expansion of the potential [Eq. (11)] is equal to the number of angles for which nonzero values of the potential were determined. This limits the expansion of V_Π and V_Σ to $0 \leq l \leq 4$, and V_2 to $2 \leq l \leq 4$. A careful check was made to ensure that this fit was smooth and did not introduce artificial maxima or minima in the R and θ dependence. The expansion coefficients of the potentials are available from the authors on request.

IV. THE POTENTIAL ENERGY SURFACES OF THE OH-Ar X AND A STATES

The calculated interaction energies for the OH-Ar X and A states are presented in Tables VI-VIII. Contour maps

TABLE VIII. CEPA(1) interaction potential V_2 (in cm^{-1}) of OH + Ar as function of R (in Å) and θ (in degrees).^a

R	θ		
	45	90	135
2.0	3173.01	5533.49	3830.26
2.5	624.58	1124.87	612.40
2.7	335.65	584.63	305.61
2.9	179.73	299.33	151.84
3.2	68.05	104.67	51.02
3.5	22.92	33.27	15.32
3.6	15.36	21.89	9.77
3.7	11.37	13.97	5.95
3.8	10.37	8.52	3.37
4.0	5.69	2.35	0.52
4.5	0.17	- 1.38	- 0.99
5.0	- 0.23	- 1.10	- 0.70
5.5	- 0.16	- 0.62	- 0.38
6.0	- 0.09	- 0.33	- 0.21
7.0	- 0.03	- 0.11	- 0.07

^a The OH bond distance is fixed at $r = 1.95$ bohr. R is the distance from the Ar atom to the center of mass of OH. θ is the angle between the r and R vectors. $\theta = 0^\circ$ and $\theta = 180^\circ$ correspond to the linear OH-Ar and Ar-OH structures, respectively.

TABLE VII. CEPA (1) interaction potential V_{11} (in cm^{-1}) of OH + Ar as function of R (in Å) and θ (in degrees).^a

R	0	45	90	135	180
1.7					54 788.84
1.8					39 734.39
1.9					28 374.91
2.0		24 575.54	15 329.87	17 314.00	20 006.06
2.1	41 558.78				13 949.22
2.3	19 477.43				6572.65
2.5	9115.35	4161.36	2384.64	2765.93	2955.55
2.6	6171.40				
2.7	4129.23	1860.91	1028.52	1193.00	
2.8	2718.79				771.15
2.9	1751.05	750.76	391.40	456.18	457.41
3.0	1092.67				250.88
3.2	355.30	105.67	33.32	44.98	33.46
3.3	163.72				
3.4					-46.54
3.5	-31.56	-62.73	-53.01	-53.25	-61.47
3.6	-73.73	-78.63	-59.41	-60.65	-67.44
3.7	-95.09	-84.33	-60.76	-62.41	-67.91
3.8	-103.22	-83.93	-59.03	-60.78	-65.17
3.9	-103.25				
4.0	-98.55	-72.08	-51.17	-52.70	-55.46
4.5	-58.65	-40.12	-29.33	-30.10	-31.02
5.0	-30.40	-21.26	-15.76	-16.18	-16.57
5.5		-11.51	-8.66	-8.93	
6.0	-8.86	-6.52	-4.98	-5.17	-5.34
7.0	-3.15	-2.41	-1.88	-1.98	-2.06

^a The OH bond distance is fixed at $r = 1.95$ bohr. R is the distance from the Ar atom to the center of mass of OH. θ is the angle between the r and R vectors. $\theta = 0^\circ$ and $\theta = 180^\circ$ correspond to the linear OH-Ar and Ar-OH structures, respectively.

of these potentials are shown in Figs. 1–3. It is seen that the A state potential (Fig. 1) has two deep minima at ($R_e = 2.9$ Å, $\theta_e = 0^\circ$) and ($R_e = 2.2$ Å, $\theta_e = 180^\circ$), corresponding to the OH-Ar and Ar-OH structures, respec-

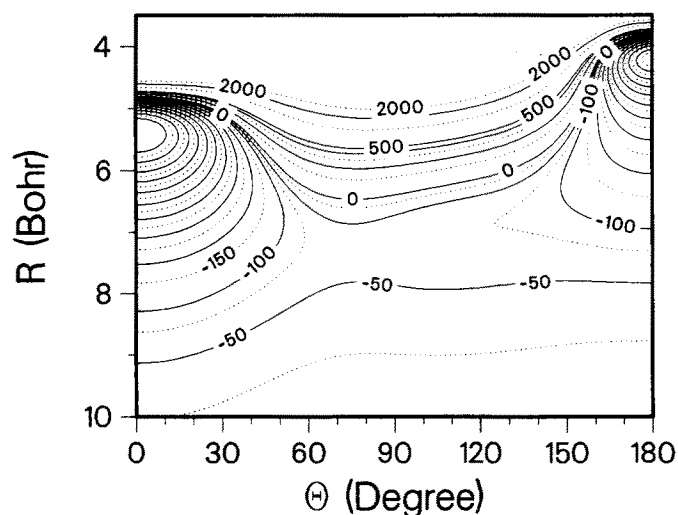


FIG. 1. Contour plot of the OH($A^2\Sigma^+$) + Ar interaction potential. Lines are drawn every 50 cm^{-1} in the range from -1100 to -100 cm^{-1} , every 25 cm^{-1} in the range from -100 cm^{-1} to 0 , every 100 cm^{-1} from 0 to 500 cm^{-1} , and every 500 cm^{-1} above 500 cm^{-1} . The plot is based on a fine grid of points obtained from the analytical fit to the calculated CEPA potential.

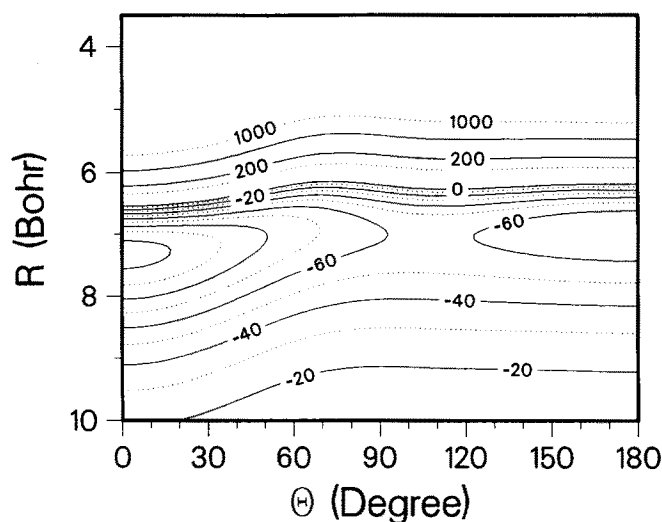


FIG. 2. Contour plot of the OH($X^2\Pi$) + Ar average interaction potential V_{11} . Lines are drawn every 10 cm^{-1} in the range from -100 cm^{-1} to 0 , and at $100, 200, 500$, and 1000 cm^{-1} . The plot is based on a fine grid of points obtained from the analytical fit to the calculated CEPA potential.

tively. The dissociation energies D_e for these two minima are calculated to be 1100 and 1000 cm^{-1} . These binding energies are about 10 times larger than those calculated for the ground state ($D_e = 100 \text{ cm}^{-1}$ at $\theta_e = 0^\circ$, $R_e = 3.8$ Å). For T-shaped structures the interaction energies of both states are quite similar; the minima of both the X and A state potentials for $\theta = 90^\circ$ lie at about $R = 3.7$ Å; the corresponding energies are 60 and 67 cm^{-1} , respectively. Hence, in the A state the linear OH-Ar and Ar-OH structures are separated by a barrier of about 1000 cm^{-1} . The long range part of the ground state interaction potential V_{11} (Fig. 2) is much more isotropic than the excited state potential; the energy difference between the minima at $\theta = 0^\circ$ and $\theta = 90^\circ$ only

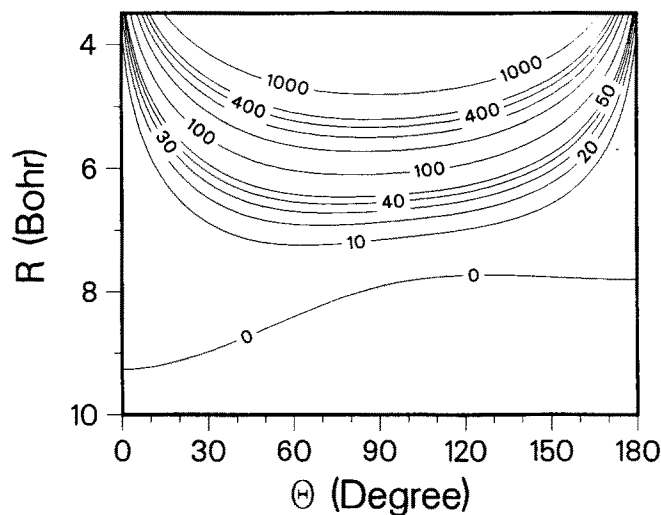


FIG. 3. Contour plot of the OH($X^2\Pi$) + Ar difference potential V_2 . Lines are drawn every 10 cm^{-1} in the range from 0 to 50 cm^{-1} , every 100 cm^{-1} in the range from 100 to 500 cm^{-1} , and at 1000 cm^{-1} . The plot is based on a fine grid of points obtained from the analytical fit to the calculated CEPA potential.

amounts to about 40 cm^{-1} . At nonlinear geometries the potentials of the two states (A' and A''), which correlate asymptotically with the $\text{OH } ^2\Pi_x$ and $^2\Pi_y$ states, are split by $2V_2(R, \theta)$. This splitting will induce transitions between the rotational levels of the two $^2\Pi$ spin-orbit manifolds.³⁸ The V_2 potential is shown in Fig. 3. As anticipated in Sec. III, V_2 is positive. In the region of the classical turning points for room temperature collisions, the V_2 potential amounts to about 200 cm^{-1} ($\theta = 90^\circ$), which is comparable to the spin-orbit constant $A_\Pi = 129 \text{ cm}^{-1}$. Therefore, significant collision induced transition probabilities between the two spin-orbit manifolds are to be expected.

It is of interest to investigate the origin of the stronger binding in the A state complex than in the X state. Generally, several effects can contribute to the binding energy. At long range, where exchange and overlap effects are negligible, the attraction is due to induction and dispersion, and can be approximated in terms of the multipole moments of OH and the dipole and quadrupole polarizabilities of OH and Ar. At short range, a simple analysis is no longer possible, since covalent and charge transfer effects will contribute to the interaction energy. However, it is still possible to obtain information about the charge distribution in the complex from the dipole moment. More detailed information can be obtained by performing a distributed multipole analysis (DMA) as proposed by Stone.³⁹

Figures 4 and 5 show cuts through the interaction potentials for collinear geometries and 0° and 180° , respectively. The full curves are the calculated potentials, while the dash and dash-dot lines are the induction and induction + dispersion energies obtained from the multipole moments and polarizabilities in Table I. The dispersion energies have been calculated from the formulas given by Buckingham,⁹ which use the Unsöld approximation. The U_1 and U_2 values are taken equal to the first ionization potentials of OH and Ar, respectively. Even though this approximation is somewhat questionable, Figs. 4 and 5 show that the long range part of the ground state potential is quite well reproduced and that the multipole expansion is valid up to close

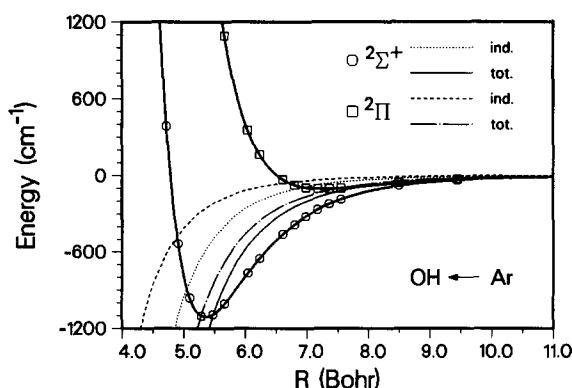


FIG. 4. Cuts through the OH-Ar interaction potentials for collinear geometry ($\theta = 0^\circ$). Full lines with markers: Calculated CEPA potentials. The dashed and dotted lines (marked ind.) are the induction energies computed from the data in Tables I and II. The dash-dot and full lines (marked tot.) are the induction plus approximate dispersion energies computed in the Unsöld approximation.

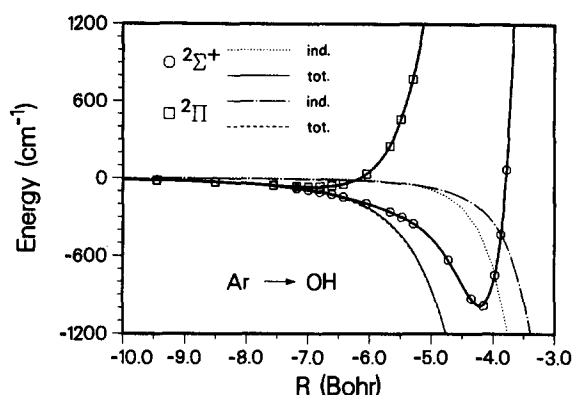


FIG. 5. Cuts through the Ar-OH interaction potentials for collinear geometry ($\theta = 180^\circ$). Full lines with markers: Calculated CEPA potentials. The dotted and dash-dot lines (marked ind.) are the induction energies computed from the data in Tables I and II. The dashed and full lines (marked tot.) are the induction plus approximate dispersion energies computed in the Unsöld approximation.

the minima of the potentials. For the excited state, however, there are substantial differences between the computed potential and the multipole expansion even at long range, which could arise in part from the inapplicability of the Unsöld approximation for the excited state, which is dipole coupled to a lower state. Moreover, the minima are at much shorter range, and in this region the long-range expansion of the potential cannot be expected to be valid. The strong binding at collinear geometries indicates that a weak covalent bond is formed by the overlapping OH 3σ and the Ar $3p_z$ orbitals. However, it should be noted that most of the bonding is due to electron correlation effects. Both in the SCF or MCSCF approximations only a small fraction of the bond energy is recovered, and the corresponding equilibrium distances are much too long. Therefore, all attempts to interpret the bonding mechanism in terms of simple molecular orbital theory are questionable.

Figures 6 and 7 show the calculated dipole moment functions (solid lines) and the dipole moments obtained from the multipole moments and polarizabilities of the frag-

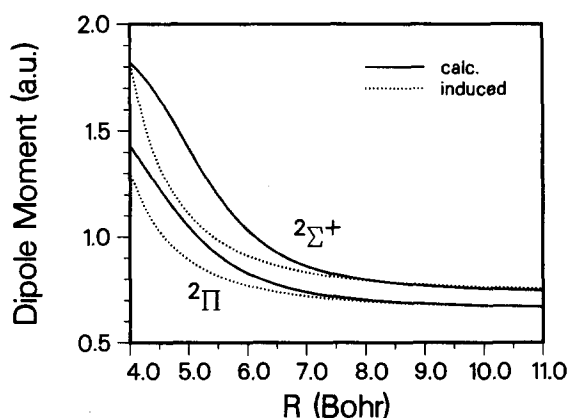


FIG. 6. Dipole moments of OH-Ar for collinear geometry ($\theta = 0^\circ$). Full line: Computed CEPA dipole moments. Dotted lines: Induced dipole moments computed from the data in Tables I and II.

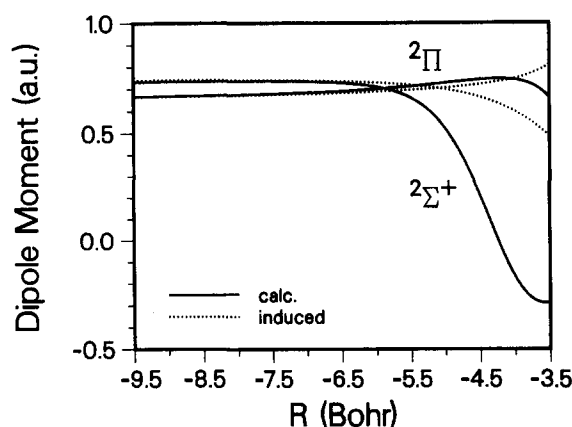


FIG. 7. Dipole moments of OH-Ar for collinear geometry ($\theta = 180^\circ$). Full line: Computed CEPA dipole moments. Dotted lines: Induced dipole moments computed from the data in Tables I and II.

ments for collinear OH-Ar and Ar-OH geometries. Qualitatively, the form of the dipole moment functions is well reproduced by the multipole approximation; very similar functions are obtained if distributed multipoles located at the O and H atoms are used instead of the multipoles at the center of mass of OH. The different shape of the dipole functions for OH-Ar (Fig. 6) and Ar-OH (Fig. 7) is caused by the large quadrupole moment of OH. At short distances, the dipole moments are more positive (OH-Ar) or negative (Ar-OH) than expected from the induction effect. This indicates some charge transfer from Ar to OH, in particular for the Ar-OH structure. In fact, as shown in Table IX, this can be quantified by a distributed multipole analysis³⁹ performed with the CEPA first order density matrix. Table IX shows that at the minimum of the Ar-OH structure the charge at the Ar atom is about +0.2 a.u., while for OH-Ar it is less than 0.1 a.u. From the data in Table IX it is possible to estimate the electrostatic energy contributions to the binding energy. It is found that for the OH-Ar structure this effect is small, while a larger contribution is obtained for the Ar-OH structure. This is due to the fact that for OH-Ar the

TABLE IX. Distributed charges q and dipole moments μ (in a.u.) for OH-Ar.

R^a	$2\Sigma^+$			2Π		
	∞	2.9	-2.2	∞	2.9	-2.2
q_{Ar}	0.0	0.0837	0.1926	0.0	0.0163	-0.0157
μ_{Ar}	0.0	0.1391	-0.0219	0.0	0.1150	0.1477
q_O	-0.3741	-0.3912	-0.5223	-0.2374	-0.2456	-0.1874
q_H	0.3741	0.3075	0.3297	0.2374	0.2294	0.2032
μ_O	-0.1854	-0.1062	-0.2430	0.0773	0.1450	-0.0822
μ_H	0.1757	0.1038	0.3432	0.1090	0.1218	0.2213
μ_{OH}^b	0.7200	0.6068	0.7662	0.6492	0.7160	0.5336
μ_{tot}	0.7200	1.2045	-0.0566	0.6492	0.9200	0.7467

^a $R = 2.9$ corresponds to OH-Ar structure, $R = -2.2$ to Ar-OH structure.

^b Dipole moments calculated from the moments at O and H with respect to the center of mass of OH, $r = 1.95$ bohr.

charge-dipole and dipole-dipole contributions largely cancel, while they are additive for the Ar-OH structure. As mentioned before, such considerations should be regarded with care, since electron exchange and overlap effects are certainly not negligible in the region of the potential energy minima.

V. SCATTERING CALCULATIONS

The *ab initio* potential energy surface for OH($A^2\Sigma^+$) + Ar has been employed in close-coupled (CC) and coupled states (CS) quantum scattering calculations of integral cross sections for rotational energy transfer in the OH $A^2\Sigma^+$ state. The theory for rotationally inelastic transitions between a diatomic molecule in a $2\Sigma^+$ state and a structureless target has been worked out in detail by Alexander⁴⁰ and Corey and McCourt.^{41,42} However, some definitions and equations used here are different from those in Alexander's original paper⁴⁰ and we will therefore briefly review the relevant aspects of this theory.

Within the Born-Oppenheimer approximation, the rovibrational states of the OH $A^2\Sigma^+$ state can be described in a Hund's case (a) basis,^{43,44} namely

$$|JM\Omega\epsilon\rangle|\Sigma v\rangle = 2^{-1/2}(|JM\Omega\rangle|\Sigma\rangle + \epsilon|JM-\Omega\rangle|-\Sigma\rangle)|v\rangle, \quad (16)$$

where J denotes the total angular momentum with projections M and $\Omega = \Sigma$ along the space and molecule fixed axis, respectively. $|\Sigma\rangle$ denotes the electronic wave function with projection $\Sigma = \pm \frac{1}{2}$ of the spin-angular momentum along the molecular axis; and $|v\rangle$ denotes the vibrational wave function of the molecule. The parity index ϵ can take the values ± 1 , and the total parity of the molecular wave function is $\epsilon(-1)^{J-1/2}$. For a $2\Sigma^+$ molecule, the $\epsilon = +1$ states are called e or F_1 levels; the $\epsilon = -1$ states are denoted as f or F_2 levels (note that in Ref. 40 this definition is reversed). The rotational angular momentum N of the nuclei is given by

$$N = J - \epsilon/2 \quad (17)$$

and in terms of N the rotational energy levels are given by⁴⁵

$$E(N, \epsilon) = N(N+1)B_v + \frac{1}{2}\epsilon\gamma[N + \frac{1}{2}(1-\epsilon)] - N^2(N+1)^2D_v + \dots \quad (18)$$

Hence, for positive γ the $\epsilon = -1$ states are lower in energy than the $\epsilon = +1$ states, opposite to what is stated in Ref. 40. In our calculations we used the values^{29,46} $B_0 = 16.9602$ cm⁻¹, $D_0 = 0.002039$ cm⁻¹, $H_0 = 8.71 \times 10^{-8}$ cm⁻¹, and $\gamma = 0.201$ cm⁻¹.

After integrating the total Hamiltonian over electronic coordinates, we obtain the Hamiltonian of nuclear motion for the atom + molecule system

$$\hat{H}(\mathbf{r}, \mathbf{R}) = -\frac{\hbar^2}{2\mu R^2} \frac{\partial}{\partial R} \left(R^2 \frac{\partial}{\partial R} \right) + \frac{\hat{L}^2}{2\mu R^2} + \hat{H}_{mol}(\mathbf{r}) + V_\Sigma(\mathbf{R}, \mathbf{r}), \quad (19)$$

where the first two terms describe the kinetic energy of the atom-molecule pair, $\hat{H}_{mol}(\mathbf{r})$ is the vibration-rotation Hamiltonian of the OH radical in the $2\Sigma^+$ state, and

$V_{\Sigma}(\mathbf{R}, \mathbf{r})$ is the electronic interaction energy of the OH–Ar system as defined in Eq. (5). In this paper we will consider only rotational transitions within the lowest vibrational state. Neglecting any coupling to higher vibrational states and integrating over the vibrational wave functions of the molecule we can replace the last two terms in Eq. (19) by $E_{v=0} + \hat{H}_{\text{rot}} + V_{\Sigma,0}(R, \theta)$, where $E_{v=0}$ is the electronic energy plus the vibrational zero point energy of the molecule, \hat{H}_{rot} is the rotational Hamiltonian of the molecule and

$$V_{\Sigma,0}(R, \theta) = \langle v=0 | V_{\Sigma}(R, \mathbf{r}, \theta) | v=0 \rangle \approx V_{\Sigma}(R, r_0, \theta) \quad (20)$$

is the vibrationally averaged interaction potential for $v=0$, which approximately equals the potential calculated at the average distance r_0 of the vibrational ground state. For the $^2\Sigma^+$ state of OH, $r_0 = 1.95 \text{ \AA}$.

The total nuclear wave function of the OH–Ar system is represented in a basis of products of the rovibrational wave

functions given in Eq. (16) and eigenfunctions $|LM_L\rangle$ of L^2 . The products are coupled to the total angular momentum \mathcal{J} with space frame projection \mathcal{M}

$$|JL\Omega\epsilon\mathcal{J}\mathcal{M}\rangle = \sum_{MM_L} (JMLM_L | \mathcal{J}\mathcal{M}) |JM\Omega\epsilon\rangle |LM_L\rangle, \quad (21)$$

where $(JMLM_L | \mathcal{J}\mathcal{M})$ are Clebsch–Gordon coefficients, and for a $^2\Sigma^+$ state $\Omega = 1/2$. If the total wave function is expanded as a linear combination of these basis functions and inserted into the Schrödinger equation of nuclear motion one obtains, after integration over the angles, the usual set of close-coupled equations. The R dependent matrix elements of the interaction potential $V_{\Sigma,0}(R, \theta)$ are blocked with respect to the total angular momentum \mathcal{J} and independent of \mathcal{M} and are given by^{31,33}

$$\begin{aligned} V_{J'L'(1/2)\epsilon\Lambda', JL(1/2)\epsilon\Lambda}(R) &= (-1)^{J'+J+J'-(1/2)} [(2J+1)(2J'+1)(2L+1)(2L'+1)]^{1/2} \\ &\times \sum_{\mathcal{J}} \begin{pmatrix} L' & l & L \\ 0 & 0 & 0 \end{pmatrix} \begin{Bmatrix} J' & L' & \mathcal{J} \\ L & J & l \end{Bmatrix} \frac{1}{2} [1 - \epsilon\epsilon'(-1)^{J+J'+l}] \\ &\times \begin{pmatrix} J' & l & J \\ -\frac{1}{2} & 0 & \frac{1}{2} \end{pmatrix} V_{\Sigma}^l(R, r_0), \end{aligned} \quad (22)$$

where $V_{\Sigma}^l(R, r_0)$ are the expansion coefficients of Eq. (5). The CC equations are propagated numerically^{47–49} from small to large R , and then the S and T matrices are obtained by applying boundary conditions using standard methods.⁵⁰ The degeneracy averaged integral cross sections are finally obtained as

$$\sigma_{J\epsilon \rightarrow J'\epsilon'} = \frac{\pi}{(2J+1)k_{J\epsilon}^2} \sum_{\mathcal{J}} (2\mathcal{J}+1) \sum_{LL'} |T_{JL\epsilon, J'L'\epsilon'}^{\mathcal{J}}|^2, \quad (23)$$

where $k_{J\epsilon}$ is the wave vector for the initial channel.

A considerable reduction in computational cost can be achieved by applying the coupled states (CS) approximation to the CC equations. In this approximation the centrifugal terms are replaced by an average centrifugal term $\hbar^2 \bar{L}(\bar{L}+1)/2\mu R^2$. Then the potential matrix can be block diagonalized by the transformation

$$|J\nu \frac{1}{2}\epsilon\mathcal{J}\mathcal{M}\rangle = (-1)^{\nu} \sum_L (2L+1)^{1/2} \times \begin{pmatrix} L & J & \mathcal{J} \\ 0 & \nu & -\nu \end{pmatrix} |JL \frac{1}{2}\epsilon\mathcal{J}\mathcal{M}\rangle, \quad (24)$$

and the potential matrix is given by

$$\begin{aligned} V_{J'\nu'(1/2)\epsilon\Lambda', J\nu(1/2)\epsilon\Lambda}(R) &= \delta_{\nu\nu'} (-1)^{\nu+\nu'+1/2} [(2J+1)(2J'+1)]^{1/2} \\ &\times \sum_L V_{\Sigma}^l(R, r_0) \end{aligned}$$

$$\begin{aligned} &\times \begin{pmatrix} J' & l & J \\ \frac{1}{2} & 0 & \frac{1}{2} \end{pmatrix} \begin{Bmatrix} J' & l & J \\ \nu & 0 & -\nu \end{Bmatrix} \\ &\times \frac{1}{2} [1 - \epsilon\epsilon'(-1)^{J+J'+1}]. \end{aligned} \quad (25)$$

The matrix elements are independent of \mathcal{J} and \mathcal{M} . The reduction in computational cost stems from the fact that in the transformed basis only channels with the same projection index ν are coupled. The degeneracy averaged integral cross sections are given by

$$\sigma_{J\epsilon \rightarrow J'\epsilon'} = \frac{\pi}{(2J+1)k_{J\epsilon}^2} \sum_{\nu} (2\nu+1) |T_{J\epsilon, J'\epsilon'}^{\nu}|^2. \quad (26)$$

Here the last sum runs only over all positive values of ν , since the sign of the T -matrix elements is independent of the sign of ν .³⁶

Table X shows a comparison of integral cross sections obtained with the CS and the CC methods. It is found that for most transitions the values differ by less than 10%. Therefore, we performed all further calculations only within the CS approximation.

The rotational basis used in the scattering calculations was comprised of states up to $N=15$, which insures that even for high collision energies some closed channels are included. By reducing the size of the basis it was found that all cross sections at least up to $N=6$ are converged. The CS equations were propagated from $R=3.5$ to $R=50$ bohr using the HIBRIDON program written by Alexander and Manolopoulos.^{47–49} Various tests on the accuracy of the numerical integration procedure indicated that the calculated CS cross

TABLE X. Comparison of integral cross sections (in \AA^2) for OH($A^2\Sigma^+$) + Ar calculated within the close-coupling (CC) and coupled states (CS) approximations.^a The initial state is $N=1$, F_1 . The total energies E_{tot} are the internal plus kinetic energies.

Final state		$E_{\text{tot}} = 355 \text{ cm}^{-1}$			$E_{\text{tot}} = 450 \text{ cm}^{-1}$		
		CC	CS	CS/CC	CC	CS	CS/CC
$N=0$	F_1	9.593	8.020	0.836	10.906	9.744	0.893
$N=1$	F_2	8.044	7.702	0.957	5.741	5.586	0.973
$N=2$	F_2	6.139	5.549	0.904	6.079	5.222	0.859
	F_1	14.522	14.450	0.995	14.118	14.00	0.992
$N=3$	F_2	2.563	2.861	1.116	2.276	2.576	1.132
	F_1	3.865	4.075	1.054	3.620	3.752	1.036
$N=4$	F_2	0.529	0.549	1.038	1.023	1.148	1.122
	F_1	0.529	0.549	1.038	1.026	1.162	1.132

^a The rotational basis included states up to $N=11$. The partial cross sections were summed up to $J=90$ in the CC calculations, and up to $L=90$ in the CS calculations.

sections are converged to better than 2%.

The cross sections were calculated for 27 collision energies in the range up to 3000 cm^{-1} . These values were then spline interpolated and rate constants computed by integration over a Boltzmann energy distribution of relative translational energies, namely

$$k_{if}(T) = \frac{1}{N} \left(\frac{8}{\pi\mu} \right)^{1/2} (kT)^{-3/2} \times \int_0^{E_{\text{max}}} \sigma(E_k) \exp\left(-\frac{E_k}{kT}\right) E_k dE_k, \quad (27)$$

where

$$N = 2\pi^{-1/2} (kT)^{-3/2} \int_0^{E_{\text{max}}} \exp\left(-\frac{E_k}{kT}\right) E_k^{1/2} dE_k. \quad (28)$$

E_k is the relative kinetic energy and μ the reduced mass of the OH-Ar system. In the above expression, the error made by restricting the upper limit of the integral to the highest energy for which the cross sections were calculated

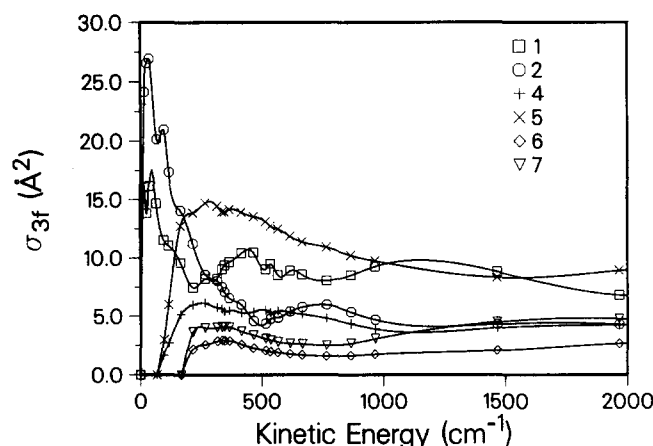


FIG. 8. Computed cross sections as function of the collision energy for rotationally inelastic transitions in OH($A^2\Sigma^+$) + Ar. The rotational levels are numbered according to increasing energy. The initial level (3) is $N=1$, F_1 , and the final levels (1-7) are the $N=0$, F_1 to $N=3$, F_1 states.

($E_{\text{max}} = 3000 \text{ cm}^{-1}$), is largely canceled by the normalization factor N in the denominator. It was found that for collision temperatures up to $T = 2500 \text{ K}$ the calculated rate constants were insensitive to the upper integration limit.

VI. RESULTS AND DISCUSSION

The calculated cross sections for a collision energy of 312 cm^{-1} are listed in Table XI; the energy dependence of the cross sections for the $N=1$, F_1 and $N=4$, F_2 initial states is shown in Figs. 8 and 9, respectively. The corresponding rate constants are listed in Table XII and their energy dependence is illustrated in Figs. 10 and 11, respectively. The cross sections as function of the collision energy exhibit strong oscillations up to a collision energy of about 1000 cm^{-1} , in particular for transitions out of the lower rotational levels (see Fig. 8). This structure is probably due to interference effects which are caused by the two deep po-

TABLE XI. Calculated integral cross sections (in \AA^2) for rotationally inelastic transitions in OH($A^2\Sigma^+$) in collisions with Ar. The collision energy is 312.8 cm^{-1} .

Final state	Initial state										
	$N = 0$	$N = 1$		$N = 2$		$N = 3$		$N = 4$		$N = 5$	
	F_1	F_2	F_1	F_2	F_1	F_2	F_1	F_2	F_1	F_2	F_1
$N = 0$ F_1		8.71	8.52	1.98	1.96	0.88	0.87	0.34	0.34	0.09	0.09
$N = 1$ F_2	7.35		7.79	7.21	3.06	1.20	1.16	0.58	0.85	0.38	0.24
F_1	14.40	15.65		7.08	11.10	2.36	2.37	1.60	1.33	0.53	0.67
$N = 2$ F_2	3.16	13.24	5.59		7.98	6.71	3.31	1.48	1.13	0.28	0.31
F_1	4.66	6.89	14.66	11.96		5.28	8.60	1.75	2.09	0.45	0.43
$N = 3$ F_2	1.47	3.35	2.96	7.73	3.96		7.68	5.69	3.76	1.86	0.96
F_1	2.01	3.76	4.17	4.93	8.75	10.22		5.14	7.02	1.32	2.24
$N = 4$ F_2		0.19	0.24	1.21	0.86	3.70	3.35		9.00	1.59	1.69
F_1		0.27	0.24	1.04	1.36	4.09	4.68	11.22		2.13	2.00
$N = 5$ F_2						0.08	0.05	0.69	0.76		12.30
F_1						0.04	0.07	0.91	0.85	14.54	
$N = 6$ F_2										0.27	0.10
F_1										0.12	0.28

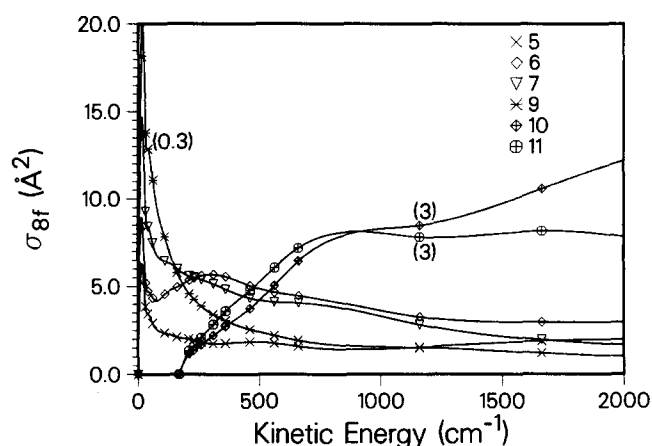


FIG. 9. Computed cross sections as function of the collision energy for rotationally inelastic transitions in OH ($A^2\Sigma^+$) + Ar. The rotational levels are numbered according to increasing energy. The initial level (8) is $N=4$, F_2 , and the final levels (5–11) are the $N=2$, F_1 to $N=5$, F_1 states. Numbers in parentheses are scaling factors of the cross sections.

tential wells. In contrast to the cross sections, the rate constants are very smooth functions of the energy (Figs. 10 and 11).

In collisions of a $^2\Sigma^+$ molecule, the electronic spin is a spectator,^{40,41} so that transitions from F_1 levels ($J=N+S$) to F_2 levels ($J=N-S$) or vice-versa can occur only through collisions which strongly reorient N . Since most collisions are glancing encounters, in which strong reorientation of N is not expected to occur, one would anticipate a large propensity for conservation of the relative orientation of N and J , and hence conservation of the F_i level.^{41,51}

In fact, for transitions out of the $N=0$, F_1 level (Table XI) we observe a significant propensity for parity-conserving transitions, i.e., $F_1 \rightarrow F_1$. Within the infinite-order sudden approximation, Alexander⁴⁰ has derived the relation

$$\sigma_{N=0, \epsilon=1 \rightarrow N, \epsilon=1} / \sigma_{N=0, \epsilon=1 \rightarrow N, \epsilon=-1} = (N+1)/N. \quad (29)$$

The cross sections in the first column of Table XI almost perfectly match this simple prediction; this is not surprising,

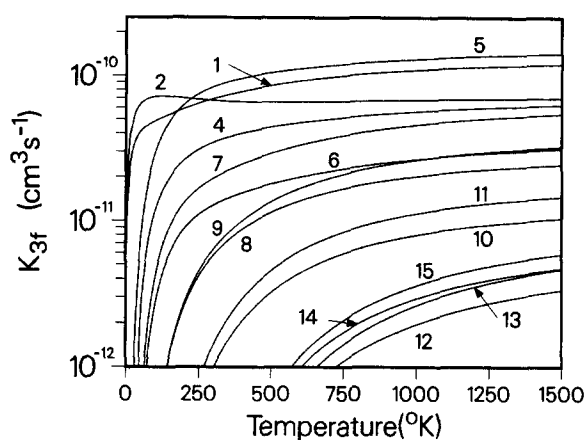


FIG. 10. Computed rate constants as function of the temperature for rotationally inelastic transitions in OH ($A^2\Sigma^+$) + Ar. The rotational levels are numbered according to increasing energy. The initial level (3) is $N=1$, F_1 , and the final levels (1–15) are the $N=0$, F_1 to $N=7$, F_1 states.

since for transitions out of the lowest level only one term in the summation in Eq. (25) contributes, and the off-diagonal matrix elements reflect the same ratios.

Another similar simple relation seen in Tables XI and XII is

$$\sigma_{N, \epsilon=-1 \rightarrow N, \epsilon=1} / \sigma_{N, \epsilon=1 \rightarrow N, \epsilon=-1} = (N+1)/N. \quad (30)$$

This scaling relation is due to microreversibility and holds since the F_1 and F_2 components of the same N are almost degenerate. However, various other IOS scaling relations given by Alexander⁴⁰ fail entirely to reproduce the computed ratios of the cross sections or rate constants. This suggests that collisions of the light hydride OH with its large rotational constant are not well described within the sudden limit. This is exacerbated in the present case because of the deep attractive potential.

For most initial levels we find the largest cross sections occur for transitions to the nearly degenerate other spin-doublet level of the same N , even though this transition

TABLE XII. Rate constants (in $10^{-11} \text{ cm}^3 \text{ s}^{-1}$) for rotationally inelastic transitions in OH($A^2\Sigma^+$) in collisions with Ar at a temperature of 300 K.

Final state	Initial state										
	$N=0$	$N=1$		$N=2$		$N=3$		$N=4$		$N=5$	
	F_1	F_2	F_1	F_2	F_1	F_2	F_1	F_2	F_1	F_2	F_1
$N=0$ F_1		7.07	6.93	1.64	1.62	0.72	0.71	0.32	0.32	0.06	0.06
$N=1$ F_2	6.00		6.76	5.06	2.05	1.22	0.89	0.50	0.63	0.25	0.17
F_1	11.78	13.50		4.81	7.72	1.90	2.18	1.23	1.08	0.37	0.44
$N=2$ F_2	2.03	7.32	3.47		6.98	4.61	2.31	1.30	0.90	0.19	0.20
F_1	3.00	4.45	8.37	10.37		3.70	5.93	1.41	1.79	0.29	0.29
$N=3$ F_2	0.82	1.64	1.28	4.28	2.22		6.65	3.58	2.70	1.29	0.70
F_1	1.08	1.59	1.96	2.85	4.89	8.80		3.67	4.52	0.96	1.55
$N=4$ F_2	0.26	0.46	0.57	0.84	0.61	2.50	1.70		7.92	1.39	1.31
F_1	0.32	0.73	0.63	0.72	0.96	2.34	2.95	9.87		1.67	1.71
$N=5$ F_2	0.03	0.13	0.10	0.07	0.07	0.50	0.28	0.78	0.70		9.77
F_1	0.03	0.11	0.14	0.09	0.08	0.33	0.54	0.88	0.92	11.69	
$N=6$ F_2	0.02	0.00	0.01	0.06	0.04	0.01	0.01	0.34	0.16	0.37	0.22
F_1	0.02	0.01	0.01	0.04	0.06	0.01	0.02	0.17	0.36	0.25	0.41

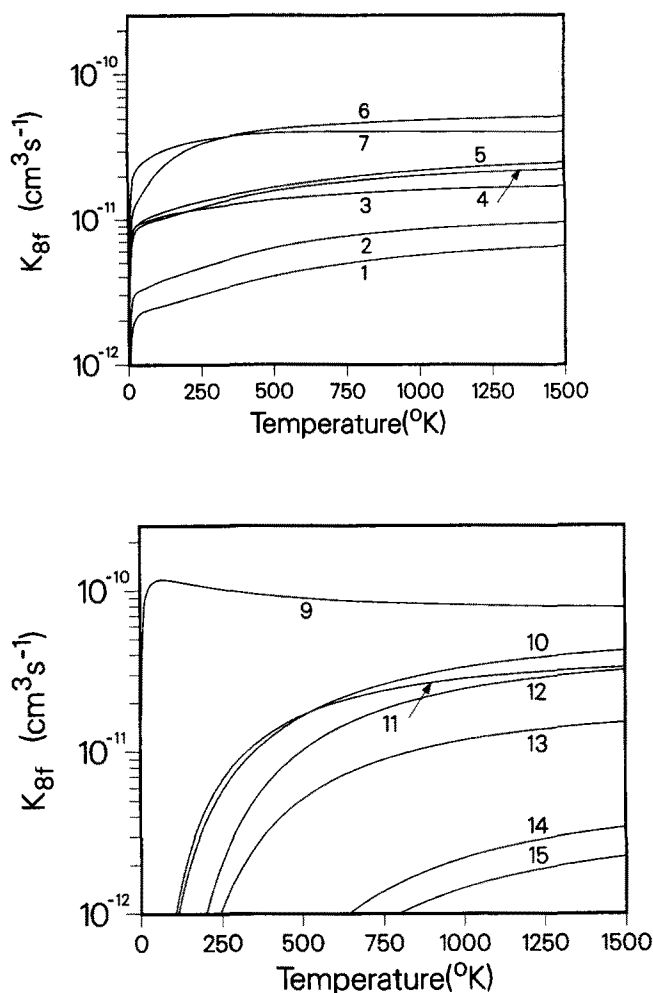


FIG. 11. Computed rate constants as function of the temperature for rotationally inelastic transitions in OH ($A^2\Sigma^+$) + Ar. The rotational levels are numbered according to increasing energy. The initial level (8) is $N = 4$, F_2 , and the final levels (1–15) are the $N = 0$, F_1 to $N = 7$, F_1 states. (a) exoergic transitions; (b) endoergic transitions.

changes the parity index. For transitions which change N we observe that parity conserving transitions are only slightly favored. In general, $\Delta N = 1$ transitions are most likely, and the cross sections decrease with increasing ΔN . This finding is distinctly different from the results of similar calculations for OH + He, which will be published in a separate paper.⁵² In the latter case the potential is much less attractive, and terms V'_l with odd l in the angular expansion of the potential [Eq. (5)] are much smaller than for OH–Ar. This results in larger cross sections for $\Delta N = 2$ transitions than for $\Delta N = 1$ transitions.

In Figs. 12 to 15 we compare our computed rate constants for $T = 300$ K to the available experimental data. In Figs. 12 and 13 the rate constants are compared for the initial $N = 1$, F_1 and $N = 4$, F_1 levels, respectively, with the experimental data of Lengel and Crosley.⁶ In both cases we find that the experimental rate constants (full circles) are less peaked at small ΔN than the calculated ones (open circles), and, furthermore, most of the experimental rate constants for small ΔN are much smaller than the theoretical values. This disagreement could be due to multiple collisions effects,

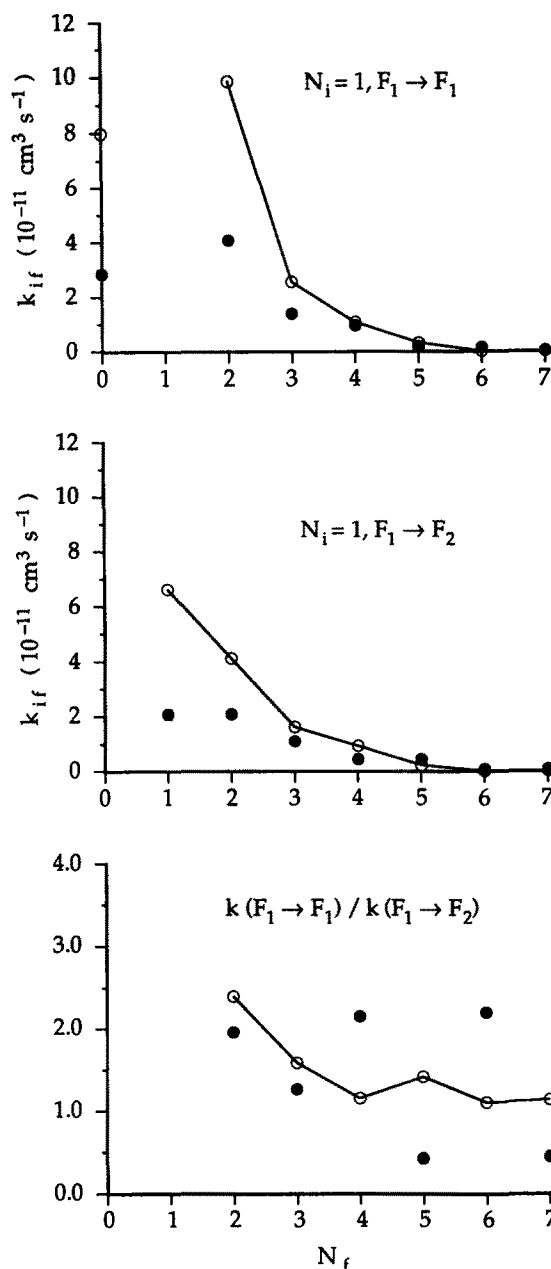


FIG. 12. Comparison of computed rate constants (open circles) with experimental rate constants (full circles) of Lengel and Crosley (Ref. 6) for the $N = 1$, F_1 initial level.

which would broaden the final state distribution and reduce the observed rate constants for small ΔN . The theoretical ratios of the $F_1 \rightarrow F_1$ and $F_1 \rightarrow F_2$ rate constants shown in the lower panels of Figs. 12 and 13 exhibit the expected preference⁴¹ for parity conserving transitions, although much less pronounced than predicted within the sudden limit. In Fig. 12 it is seen that this propensity decreases with increasing ΔN . The corresponding experimental ratios taken from the data of Lengel and Crosley⁶ show a large irregular scatter, and it is hardly possible to draw any conclusions from a comparison with these experimental data.

In Figs. 14 and 15 our calculated rate constants are compared with recent time resolved LIF measurements of Jörg *et al.*⁷ In this case the agreement between theory and experi-

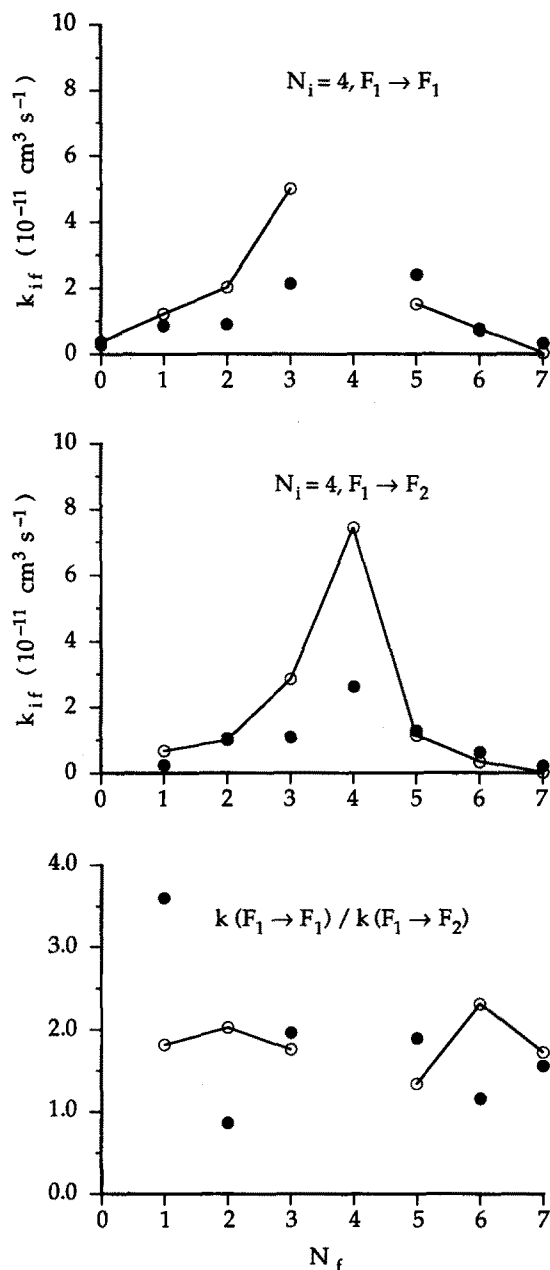


FIG. 13. Comparison of computed rate constants (open circles) with experimental rate constants (full circles) of Lengel and Crosley (Ref. 6) for the $N = 4, F_1$ initial level.

ment is much better than for the old measurements of Lengel and Crosley. In particular, the agreement for the $N = 4, F_2 \rightarrow N, F_1$ transitions shown in the middle panel of Fig. 14 is excellent; both theory and experiment exhibit the marked peaking of the rate constants for $\Delta N = 0$. Somewhat surprisingly, the calculations predict that for transitions to low N states parity changing transitions are preferred (see lower panels of Figs. 14 and 15), while for transitions to higher N states the opposite is true. The same trend is observed for the experimental rate constants, but unfortunately no experimental data are available for transitions to the $N = 6$ and $N = 7$ final states.

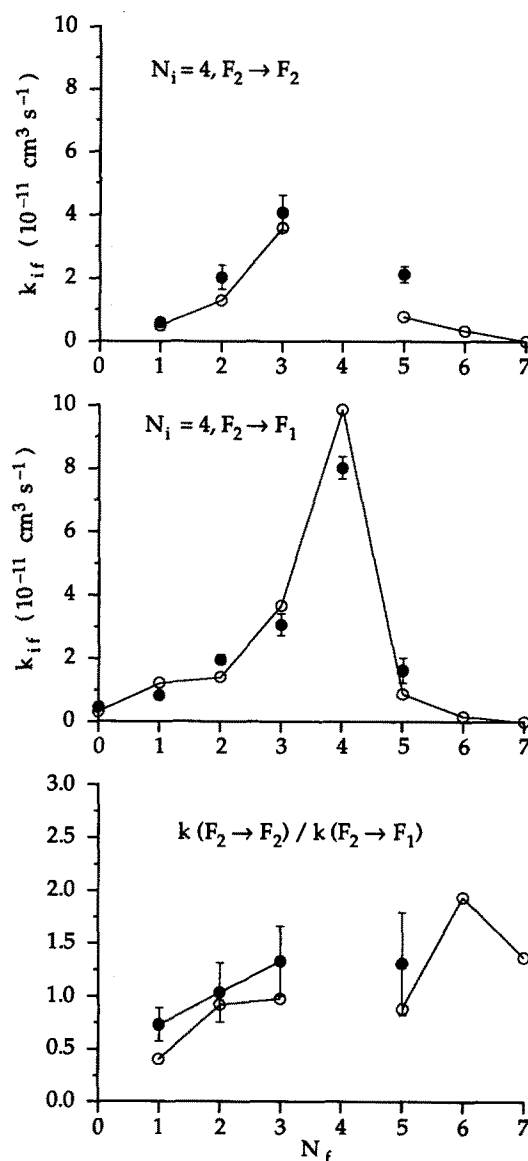


FIG. 14. Comparison of computed rate constants (open circles) with experimental rate constants (full circles) of Jörg *et al.* (Ref. 7) for the $N = 4, F_2$ initial level. The error bars indicate two standard deviations of the experimental values.

VII. SUMMARY

We have computed *ab initio* interaction potential energy surfaces for the OH ($X^2\Pi$, $A^2\Sigma^+$) + Ar system, using a large AO basis set and highly correlated CEPA electronic wave functions. The OH ($A^2\Sigma^+$)-Ar van der Waals complex is predicted to bound by about 1100 cm^{-1} , with two distinct potential energy minima corresponding to the linear OH-Ar and Ar-OH structures. To a large extent the binding is due to electron correlation effects; both the SCF or the MCSCF approximations recover only a small part of the binding energy. It is therefore likely that the calculation still underestimates the binding energy. The potential energy surface of the A state has been employed in quantum scattering calculations of cross sections for collision induced rotationally inelastic transitions in the OH $A^2\Sigma^+$ state. From

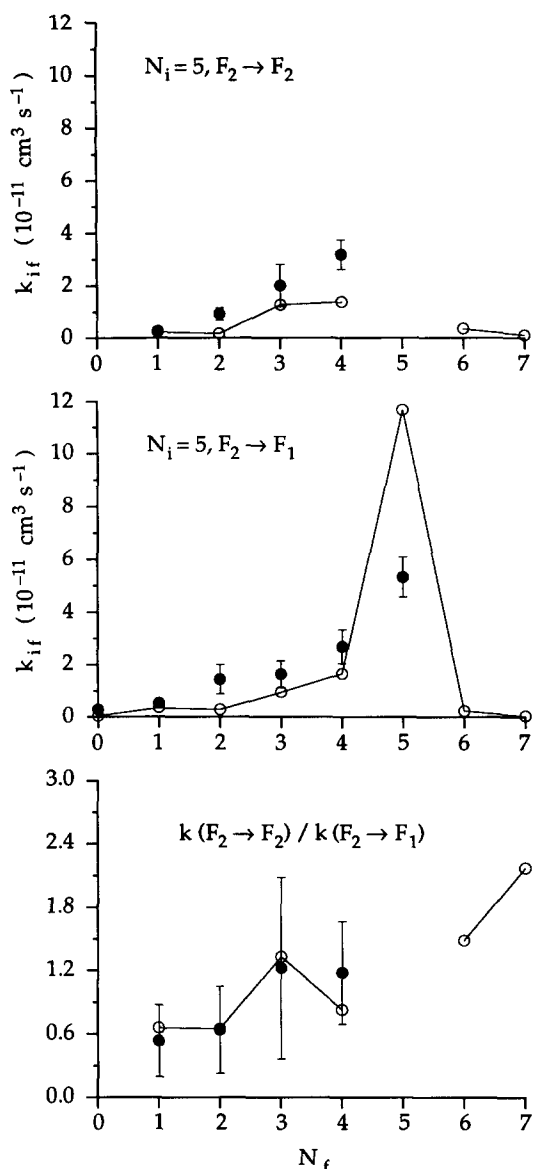


FIG. 15. Comparison of computed rate constants (open circles) with experimental rate constants (full circles) of Jörg *et al.* (Ref. 7) for the $N = 5$, F_2 initial level. The error bars indicate two standard deviations of the experimental data.

the energy dependent cross sections rate constants as function of the temperature have been computed and compared to the available experimental data. The agreement between the calculated rate constants and old measurements of Lengel and Crosley⁶ is quite poor, but excellent agreement is obtained with recent experimental data of Jörg, Meier, and Kohse-Höinghaus.⁷ In a collaborative study⁸ the same surface has been used to compute the bound rovibrational states of the OH-Ar complex in the X and A states. These calculations allow a direct comparison with recent precise spectroscopic data¹⁻³ for the A state complex, and thus give independent information about the quality of the potential. It will be shown that the computed well depth of the van der Waals complex is probably about 100 cm^{-1} (10%) too small, and that theoretical and experimental ΔG values between low lying stretching modes of the van der Waals com-

plex agree within 10%–15%. In view of the extremely large correlation effects this agreement can be regarded as quite satisfactory. Further calculations which take into account the OH vibrational coordinate in order to describe vibrationally inelastic transitions and vibrational predissociation of the OH-Ar complex are in progress.

ACKNOWLEDGMENTS

The authors would like to thank M. H. Alexander for providing his HIBRIDON scattering program and many helpful discussions. The calculations reported in this paper were performed on the CRAY-YMP832 of the Höchstleistungsrechenzentrum Jülich. This work was supported by the Deutsche Forschungsgemeinschaft, the German Fonds der Chemischen Industrie, and the Italian Consiglio Nazionale delle Ricerche.

- ¹ M. T. Berry, M. R. Brustein, J. R. Adamo, and M. Lester, *J. Phys. Chem.* **92**, 5551 (1988).
- ² M. T. Berry, M. R. Brustein, and M. Lester, *Chem. Phys. Lett.* **153**, 17 (1988).
- ³ W. Fawzi and M. C. Heaven, *J. Chem. Phys.* **89**, 7030 (1988).
- ⁴ J. Goodman and L. E. Brus, *J. Chem. Phys.* **67**, 4858 (1977).
- ⁵ J. L. Lemaire, W. L. Tchong-Brillet, N. Shafizadeh, F. Rostas, and J. Rostas, *J. Chem. Phys.* **91**, 6657 (1989).
- ⁶ R. K. Lengel and D. R. Crosley, *J. Chem. Phys.* **67**, 2085 (1977).
- ⁷ A. Jörg, U. Meier, and K. Kohse-Höinghaus, *J. Chem. Phys.* (submitted).
- ⁸ C. Chakravarty, D. C. Clary, A. Degli Esposti, and H.-J. Werner, *J. Chem. Phys.* (submitted).
- ⁹ A. D. Buckingham, *Adv. Chem. Phys.* **12**, 107 (1967).
- ¹⁰ H.-J. Werner and W. Meyer, *Mol. Phys.* **31**, 855 (1976).
- ¹¹ F. B. van Duijneveldt, IBM Research Report RJ 945 (1971).
- ¹² H. Partridge, *J. Chem. Phys.* **90**, 1043 (1989).
- ¹³ S. I. Chu, M. Yoshimine, and B. Liu, *J. Chem. Phys.* **61**, 5389 (1974).
- ¹⁴ E. M. Weinstock and R. N. Zare, *J. Chem. Phys.* **58**, 4319 (1973).
- ¹⁵ E. A. Scarl and F. W. Dalby, *Can. J. Phys.* **49**, 2825 (1971).
- ¹⁶ W. Meyer, *Int. J. Quantum Chem. Symp.* **5**, 341 (1971).
- ¹⁷ W. Meyer, *J. Chem. Phys.* **58**, 1017 (1973).
- ¹⁸ W. Meyer, *Theor. Chim. Acta* **35**, 277 (1974).
- ¹⁹ W. Meyer and P. Rosmus, *J. Chem. Phys.* **63**, 2356 (1975).
- ²⁰ H.-J. Werner, P. Rosmus, and E.-A. Reinsch, *J. Chem. Phys.* **79**, 905 (1983).
- ²¹ S. R. Langhoff, H.-J. Werner, and P. Rosmus, *J. Mol. Spectrosc.* **118**, 507 (1986).
- ²² D. R. Johnstone, G. J. Oudemans, and R. H. Cole, *J. Chem. Phys.* **33**, 1310 (1960).
- ²³ A. Dalgarno and A. E. Kingstone, *Proc. R. Soc. London Ser. A* **259**, 424 (1960).
- ²⁴ R. R. Teachout and R. T. Pack, *Atomic Data* **3**, 195 (1971).
- ²⁵ I. Cernusak, G. H. F. Diercksen, and A. J. Sadlej, *Chem. Phys. Lett.* **128**, 18 (1986).
- ²⁶ E. A. Reinsch and W. Meyer, *Phys. Rev. A* **14**, 915 (1976).
- ²⁷ S. F. Boys and F. Bernardi, *Mol. Phys.* **19**, 553 (1970).
- ²⁸ H.-J. Werner and P. J. Knowles, *J. Chem. Phys.* **89**, 5803 (1988).
- ²⁹ K. P. Huber and G. Herzberg, *Constants of Diatomic Molecules* (Van Nostrand Reinhold, Princeton, 1979).
- ³⁰ R. L. Kelly and D. E. Harrison, Jr., *Atomic Data* **3**, 177 (1971).
- ³¹ M. H. Alexander and G. C. Corey, *J. Chem. Phys.* **84**, 100 (1986).
- ³² H.-J. Werner, B. Follmeg, and M. H. Alexander, *J. Chem. Phys.* **89**, 3139 (1988).
- ³³ H.-J. Werner, B. Follmeg, M. H. Alexander, and D. Lemoine, *J. Chem. Phys.* **91**, 5425 (1989).
- ³⁴ P. J. Dagdigan, M. H. Alexander, and K. Liu, *J. Chem. Phys.* **91**, 839 (1989).

- ³⁵ M. H. Alexander, J. Chem. Phys. **76**, 5974 (1982).
³⁶ T. Orlikowski and M. H. Alexander, J. Chem. Phys. **79**, 6006 (1983).
³⁷ M. H. Alexander and P. J. Dagdigian, J. Chem. Phys. **80**, 4325 (1984).
³⁸ M. H. Alexander and S. L. Davis, J. Chem. Phys. **78**, 6754 (1983).
³⁹ A. J. Stone, Chem. Phys. Lett. **83**, 233 (1981).
⁴⁰ M. H. Alexander, J. Chem. Phys. **76**, 3637 (1982).
⁴¹ G. C. Corey and F. R. McCourt, J. Phys. Chem. **87**, 2723 (1983).
⁴² G. C. Corey, J. Chem. Phys. **81**, 2678 (1984).
⁴³ G. Herzberg, *Spectra of Diatomic Molecules*, 2nd ed. (Van Nostrand, Princeton, 1968).
⁴⁴ R. N. Zare, A. L. Schmeltekopf, W. J. Harrop, and D. L. Albritton, J. Mol. Spectrosc. **46**, 37 (1973).
⁴⁵ A. J. Kotlar, R. W. Field, J. I. Steinfeld, and J. A. Coxon, J. Mol. Spectrosc. **80**, 86 (1980).
⁴⁶ E. A. Moore and W. G. Richards, Phys. Scr. **3**, 223 (1971).
⁴⁷ M. H. Alexander, J. Chem. Phys. **81**, 4510 (1984).
⁴⁸ D. E. Manolopoulos, J. Chem. Phys. **85**, 6425 (1986).
⁴⁹ M. H. Alexander and D. E. Manolopoulos, J. Chem. Phys. **86**, 2044 (1987).
⁵⁰ D. Secrest, in *Atom-Molecule Collision Theory: A Guide for the Experimentalist*, edited by R. B. Bernstein (Plenum, New York, 1979), p. 265.
⁵¹ M. H. Alexander, S. L. Davis, and P. J. Dagdigian, J. Chem. Phys. **83**, 556 (1985).
⁵² A. Jörg, A. Degli Esposti, and H.-J. Werner, J. Chem. Phys. (submitted).